MATERIALS CHEMISTRY FRONTIERS

CHINESE CHEMICAL SOCIETY

ROYAL SOCIETY OF CHEMISTRY

RESEARCH ARTICLE

View Article Online
View Journal

Cite this: DOI: 10.1039/d6qm00098c

Dithiafulvenyl-substituted triazolobenzothiadiazines as a new family of multifunctional chromophores

Fatemeh Salami,[a] Kaijie Ni,*[b] Hojat Farshi,[a] Bing Chen[c] and Yuming Zhao*[a]

This work investigates a new class of organic π-chromophores which contain an electron-donating 1,4-dithiafulvenyl group in conjugation with an electron-withdrawing 8*H*-benzo[*e*][1,2,4]triazolo[3,4-*b*][1,3,4]-thiadiazin-8-one core in their molecular structures. The synthesis of these compounds used a phosphite-promoted olefination reaction as a key step, through which 1,3-dithiole-2-thione was reacted with corresponding benzotriazolothiadiazinone counterparts to form a flat polycyclic π-framework, allowing electron push–pull effects to occur. The resulting donor–acceptor chromophores were found to exhibit significant intramolecular charge-transfer (ICT) properties, giving strong absorption in the visible region of the spectrum. The triazolyl unit in these molecules can be protonated by strong acids to show enhanced ICT effects, while electrochemical analysis revealed that these compounds possess amphoteric behavior with tunable band gaps (*ca.* 1.3–1.4 eV) and are potentially useful organic semiconductors. We also demonstrated that this type of chromophore can be readily functionalized on the surface of TiO_2 nanoparticles without losing absorption performance. Finally, the dithiafulvenyl group incorporated in the molecular structure was found to enhance antibacterial activity, rendering the chromophores potential candidates for antibacterial/antimicrobial coatings.

Received 5th February 2026,
Accepted 6th June 2026

DOI: 10.1039/d6qm00098c

rsc.li/frontiers-materials

Introduction

Organic dyes and pigments constitute a vital class of industrial products with extensive applications across numerous scientific and engineering disciplines.[1–4] In materials science, these compounds serve as active components in various optoelectronic devices, including chemical sensors,[5–7] dye-sensitized solar cells (DSSCs),[8–10] optical data storage systems,[11] photocatalytic assemblies,[12–14] organic light-emitting diodes (OLEDs),[15–17] and field-effect transistors (FETs).[18,19] In the biomedical field, functional organic dyes enable advanced diagnostic and theranostic techniques, such as photodynamic therapy,[20] photothermal therapy,[21,22] and imaging-guided phototherapy.[23,24] A prevalent design strategy for such functional dyes is based on the electron donor–acceptor (push–pull) concept. This approach involves integrating electron-donating (D) and electron-accepting (A) groups within a molecular framework *via* π-conjugated bridges.[25–28] This molecular architecture provides exceptional tunability of electronic and optical properties, facilitating the development of chromophores and fluorophores that absorb and/or emit in the visible to near-infrared (Vis–NIR) spectral region. Consequently, push–pull organic dyes exhibiting pronounced intramolecular charge-transfer (ICT) characteristics are increasingly prominent in contemporary research on organic optoelectronic materials and devices.[29–33]

1,4-Dithiafulvene (**DTF**) is a five-membered heterocycle that functions as a versatile organic π-donor for constructing advanced optoelectronic materials.[34–37] A notable feature of **DTF** is its proaromatic character, which imparts aromatic stabilization to its oxidized state (Fig. 1A). This property underpins the excellent redox activity observed in numerous **DTF**-containing π-systems.[34] When conjugated with a π-acceptor, **DTF** can form an effective push–pull molecular system, enhancing π-electron delocalization across the donor–acceptor framework. Fig. 1B illustrates representative push–pull chromophores featuring a **DTF**–π–A motif. In these structures, a *para*-quinodimethane (***p*-QDM**) unit serves as a non-aromatic π-bridge linking the donor and acceptor groups. The resonance scheme in Fig. 1B reveals the origin of the favored π-delocalization; that is, one of the π-delocalized resonance contributors exhibits double aromaticity.

In the literature, ketone, cyanoimine, malononitrile, and barbituric-type units have been employed as π-acceptors

[a] *Department of Chemistry, Memorial University of Newfoundland, St. John's, Newfoundland, A1C 5S7, Canada. E-mail: yuming@mun.ca; Fax: +1 709 864 3702; Tel: +1 709 864 8747*
[b] *College of Chemistry and Materials Engineering, Zhejiang Agriculture & Forestry University, Hangzhou, Zhejiang, 311300, China. E-mail: nikaijie@zafu.edu.cn*
[c] *Northern Region Organic Pollution Control (NRPOP) Laboratory, Faculty of Engineering and Applied Science, Memorial University of Newfoundland, St. John's, NL A1B 3X5, Canada. E-mail: bchen@mun.ca*

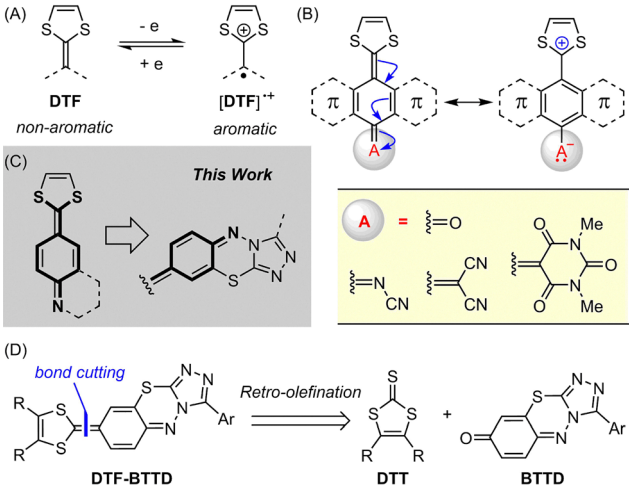

Fig. 1 (A) Single-electron transfer of **DTF**. (B) Representative push–pull systems with a **DTF** donor in conjugation with an electron-accepting group through a *p*-quinodimethane (***p*-QDM**) linkage. (C) Our designed push–pull motif where a DTF group is conjugated with an aza-quinone methide group. (D) Our target **DTF-BTTD** chromophores and their retrosynthesis.

conjugated with **DTF** to generate push–pull organic chromophores.[38–41] In contrast, imines (Schiff bases) remain relatively unexplored in this context, despite being a versatile class of molecular building blocks. Imines are readily accessible *via* simple condensation reactions and can be easily modified through interactions with acids or metal ions. They impart structural, chemical, and photochemical functionalities valuable for diverse molecular materials, including functional ligands, receptors, catalysts, molecular cages, and covalent organic frameworks (COFs).[42–47] In organic dyes, the imine unit has frequently been utilized for π-extension and to enhance electronic communication.[48–51]

In this work, we developed a new class of push–pull organic chromophores based on **DTF** (as donor) and imine-containing heterocycles (as acceptors). Fig. 1C illustrates our designed π-conjugated framework, which integrates a **DTF** group and an imine group *via* a quinoid π-bridge.[52] To ensure stability for material applications–addressing the susceptibility of simple imines to nucleophilic attack (*e.g.*, hydrolysis) and facile *E*/*Z* isomerization–we embedded the imine (C=N) bond within a π-heterocycle. A survey of the literature led us to an interesting yet underdeveloped heterocyclic system: 8*H*-benzo[*e*][1,2,4]-triazolo[3,4-*b*][1,3,4]thiadiazin-8-one (herein abbreviated as **BTTD**). This heterocyclic scaffold can be conveniently prepared *via* a high-yielding condensation approach. First reported in the early 1990s,[53,54] the **BTTD** scaffold was not recognized as useful for materials science until a recent machine learning (ML)-aided synthetic study by Jensen *et al.*[55] In that work, 44 **BTTD** derivatives were predicted by ML generative algorithms as unprecedented dye-like molecules and subsequently synthesized using an automated design-make-test-analyze (DMTA) platform.

Particularly attractive to us is the potential to extend the **BTTD** scaffold into a **DTF-BTTD** system containing the desired **DTF**–imine push–pull motif. As shown in Fig. 1D, the **DTF-BTTD** system can be synthesized *via* an olefination reaction between **BTTD** and 1,3-dithiole-2-thione (**DTT**).[56] This molecular architecture represents a significant advancement in chromophore design, offering a versatile platform that integrates multiple functionalities. First, the interplay between the **DTT** donor and the **BTTD** acceptor promotes strong intramolecular charge transfer (ICT), enhancing absorptivity in the visible to near-infrared (Vis-NIR) region. Second, the versatile reactivity and inherent pharmacological properties of the **BTTD** motif provide opportunities for flexible tunability, ligand performance, and specific biological activities. These combined properties are advantageous for advanced optoelectronic and biomedical applications. We herein report a comprehensive study of a series of **DTF-BTTD** derivatives as new multifunctional organic chromophores, encompassing their synthesis, chemical properties, visible-light absorption, interactions with acids and metal oxide nanoparticles, and biological activities.

Results and discussion

Synthesis of DTF-BTTD chromophores

Our synthesis of **DTF-BTTD** compounds commenced with the preparation of a series of 4-amino-4*H*-1,2,4-triazole-3-thiol derivatives (**1a–h**, Scheme 1) according to reported procedures.[53,54] In these structures, the 5-position of the triazole ring bears a phenyl or substituted phenyl group. Compounds **1a–h** were condensed with 1,4-benzoquinone in ethanol to afford the corresponding **BTTD** derivatives **2a–h** in good yields (80–95%). Subsequent olefination of compounds **2a–h** with 1,3-dithiole-2-thione (**3**)[57,58] in the presence of excess triethyl phosphite ($P(OEt)_3$) at 90 °C yielded the target **DTF-BTTD** compounds **4a–h** in moderate to good yields (62–74%). Overall, this synthetic route is concise, high-yielding, and readily scalable.

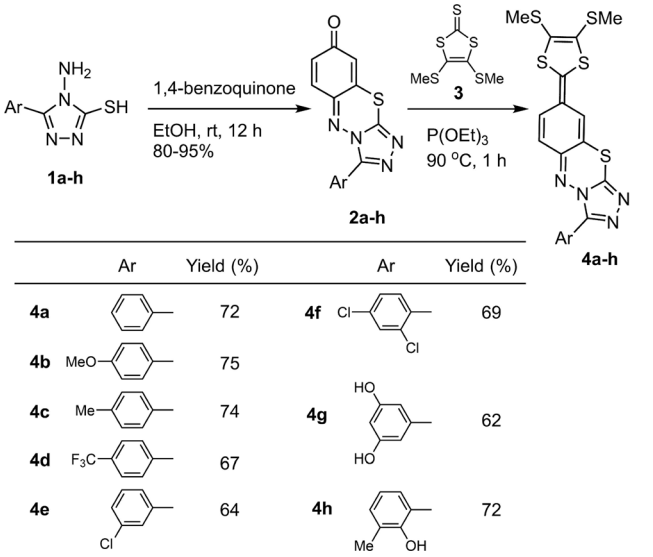

Scheme 1 Synthesis of **DTF-BTTD** chromophores **4a–h**.

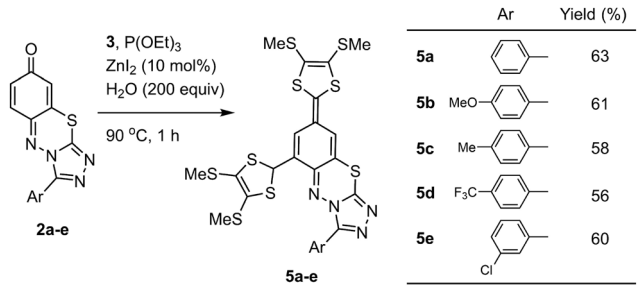

Scheme 2 Synthesis of dithiole-substituted **DTF-BTTD** derivatives **5a–e**.

During some of the olefination reactions described above, an unexpected byproduct was observed. Careful silica gel column chromatography enabled the isolation of these byproducts in pure form, and their structures were identified as **DTF-BTTD** derivatives **5** (Scheme 2). These compounds arise from a substitution reaction that attaches an additional 1,3-dithiole group to the benzo unit of the **DTF-BTTD** framework. The formation of this byproduct was more prominent when reactant **3** was not thoroughly purified after its synthesis. Given that the preparation of **3** involves zinc salts as precursors,[57] we hypothesized that residual zinc(II) in the olefination reaction promoted a subsequent substitution step. To test this hypothesis, we conducted olefination reactions between **2a–e** and **3** in the presence of varying amounts of zinc iodide and water. The optimal conditions for producing the dithiole-substituted **DTF-BTTD** compounds were achieved using zinc(II) iodide (10 mol%) and water (*ca.* 200 equiv.). Under these conditions, we successfully synthesized dithiole-substituted **DTF-BTTD** derivatives **5a–e** as the major products in satisfactory yields (56–63%, Scheme 2).

Scheme 3 outlines a proposed mechanism for the substitution reaction on the **DTF-BTTD** substrate. In this pathway, 1,3-dithiole-2-thione (**3**) first reacts with $P(OEt)_3$ in the presence of ZnI_2 and water to generate a dithiolium intermediate (**IM-1**). Within the **DTF-BTTD** structure, the carbon atom at the β-position relative to the **DTF** group is electron-rich and nucleophilic due to resonance effects. This activated β-carbon attacks the electrophilic dithiolium cation **IM-1** in a straightforward addition step, forming intermediate **IM-2**. A final, facile deprotonation then affords the dithiole-substituted product **5**. This unexpected synthetic outcome can be attributed to the pronounced intramolecular charge transfer (ICT) between the **DTF** and **BTTD** units, which significantly enhances the nucleophilicity of the benzo ring in the **BTTD** moiety.

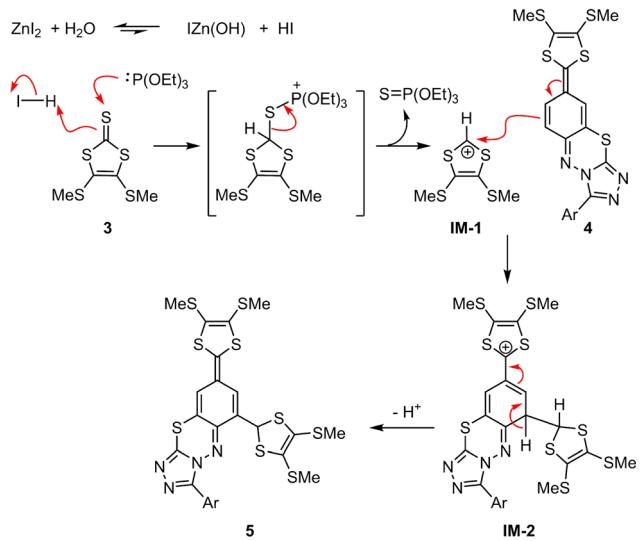

Scheme 3 Proposed mechanism for the formation of dithiole-substituted **DTF-BTTD**s.

X-ray structural properties of DTF-BTTD derivatives

The molecular structures of **DTF-BTTD** derivatives **4a–h** and **5a–e** were confirmed by NMR, IR, and MS analyses (see the supplementary information (SI) for details). All these compounds exhibit good solubility in chlorinated solvents (*e.g.*, CH_2Cl_2 and $CHCl_3$) and dipolar aprotic organic solvents (*e.g.*, acetone, acetonitrile, DMF, and DMSO). During purification, single crystals suitable for X-ray diffraction analysis were obtained for several derivatives. Single-crystal X-ray diffraction (SCXRD) analyses were subsequently performed to unambiguously determine their molecular structures and elucidate their packing arrangements in the solid state.

Fig. 2 shows the molecular structures of **4a–c**, **4h**, and **5c**, with selected geometric parameters provided in Table 1 for comparative analysis. The structure of **4a** (Fig. 2A) reveals a nearly coplanar arrangement between the **DTF** ring and the **BTTD** moiety, a geometry that facilitates π-electron delocalization across the entire conjugated framework. In contrast, the phenyl group attached to the triazole unit is rotated out of the **BTTD** plane by a torsion angle of 16.9°. For other **DTF-BTTD** derivatives bearing different substituents on the phenyl ring, the core **DTF-BTTD** structure shows minimal variation compared to **4a** (Table 1), indicating that substituent effects on the molecular geometry are negligible. The torsion angles between the phenyl rings and their respective **BTTD** units, however, vary among these compounds. Notably, compound **4h** features an intramolecular hydrogen bond between the *ortho*-hydroxy group and the N3 atom of the triazole ring, with an N3···H1 distance of 1.86 Å and an N3···H1–O1 angle of 146.1° (see Fig. 2E for atomic labeling). This interaction enforces coplanarity between the phenyl ring and the **BTTD** unit in **4h**.

Single crystals were also obtained upon protonation of compound **4b** with trifluoroacetic acid (TFA). Fig. 2C shows the molecular structure of the resulting $[\mathbf{4b} + H]^+$ salt, confirming protonation at the N3 position of the triazole unit. The triazolium cation co-crystallizes with a trifluoroacetate counterion and a neutral TFA molecule. This structure clearly demonstrates that the N3 site of **4b** is more basic than other nitrogen atoms in the **BTTD** framework, rendering it more susceptible to interaction with acidic species. Following protonation, the anisole group of **4b** adopts a more coplanar orientation relative to the **BTTD** unit compared to the neutral molecule. This conformation facilitates π-electron delocalization between the anisole (donor) and triazolium (acceptor) rings.

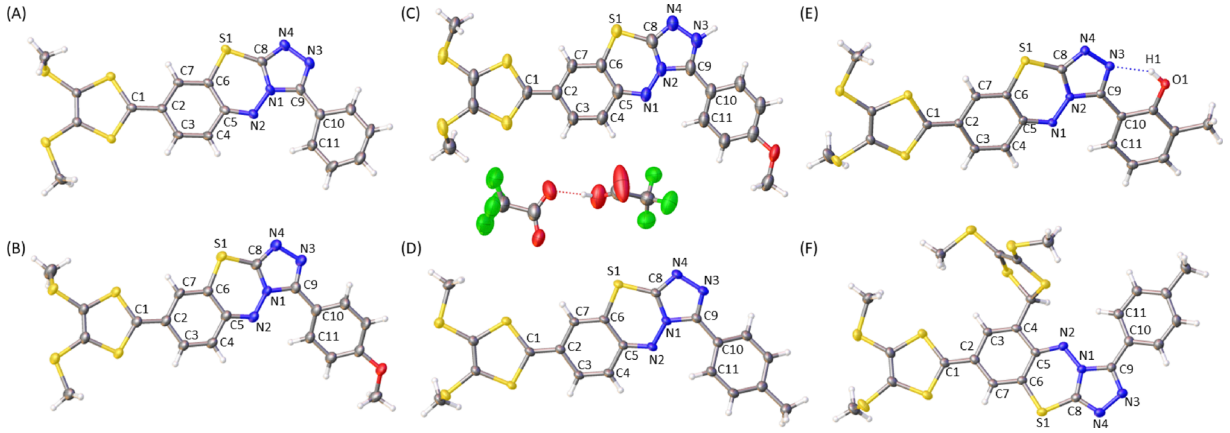

Fig. 2 ORTEP drawings (at 50% ellipsoid probability) of the molecular structures of (A) **4a**, (B) **4b**, (C) [**4b** + H^+][CF_3COO^-], (D) **4c**, (E) **4h**, and (F) **5c**.

Table 1 Selected bond lengths (in Å) and torsion angles (φ, in deg) for **4a**, **4b**, [**4b** + H^+], **4c**, **4h**, **5c**, and **6**

Entry	4a	4b	[4b + H+]	4c	4h	5c	6
C1–C2	1.39	1.40	1.39	1.39	1.39	1.40	1.39
C2–C3	1.43	1.43	1.42	1.44	1.43	1.43	1.43
C3–C4	1.35	1.35	1.38	1.36	1.35	1.35	1.34
C4–C5	1.44	1.44	1.42	1.44	1.44	1.45	1.44
C5–C6	1.45	1.45	1.44	1.45	1.45	1.46	1.42
C6–C7	1.36	1.36	1.38	1.37	1.36	1.36	1.37
C7–C2	1.44	1.43	1.41	1.43	1.43	1.42	1.43
C5–N1	1.32	1.31	1.33	1.32	1.32	1.31	1.31
C6–S1	1.77	1.76	1.77	1.77	1.77	1.77	1.77
φ^a	16.9	29.1	3.6	31.9	10.3	7.2	10.5

[a] φ is the torsion angle across N2–C9–C10–C11.

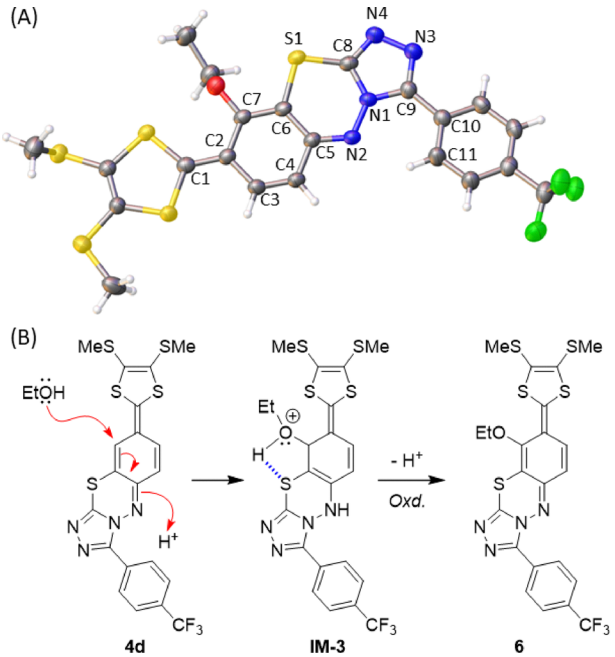

Fig. 3 (A) ORTEP drawing (at 50% ellipsoid probability) of the molecular structure of compound **6**. (B) Proposed mechanism for the formation of **6**.

The X-ray structure of the dithiole-substituted derivative **5c** is shown in Fig. 2F. Its π-conjugated backbone exhibits a geometry very similar to that of the other **DTF-BTTD** systems (Table 1). The dithiole ring attached at the C4 position experiences minimal steric clash with neighboring groups and consequently has little influence on the conformation or π-conjugation of the **DTF-BTTD** core. In the solid state, however, the dithiole group facilitates intermolecular N···S interactions, promoting a slipped face-to-face stacking arrangement in the crystal structure of **5c**.

During attempts to grow single crystals of compound **4d** by antisolvent vapor diffusion using ethanol, X-ray analysis of the resulting crystals surprisingly revealed the structure of a new compound, **6** (Fig. 3A). In **6**, an ethoxy group is bonded to the benzo moiety of **BTTD** at the C7 position. The formation of **6** under these crystallization conditions can be rationalized by the mechanism outlined in Fig. 3B. We propose that the electron-withdrawing trifluoromethyl (CF_3) group in **4d**, combined with trace acids in solution, enhances the electrophilicity of the substrate. Ethanol then acts as a nucleophile, attacking **4d** *via* a conjugate addition. The observed regioselectivity is attributed to favorable hydrogen bonding between the ethanol proton and a sulfur atom in the thiadiazine unit. This addition yields intermediate **IM-3**, which is subsequently oxidized by ambient oxygen to afford the ethoxy-substituted product **6**. Similar to **5c**, the π-conjugated backbone of **6** shows minimal geometric deviation from other **DTF-BTTD** structures (Table 1).

Crystal packing properties of DTF-BTTD derivatives

X-ray analysis reveals that all **DTF-BTTD** derivatives possess a planar π-conjugated skeleton and extended flat π-surfaces, structural features that favor intermolecular π-stacking in the solid state. The detailed π-stacking motifs observed in their single-crystal structures are summarized in Fig. 4. These compounds generally pack with either parallel or antiparallel molecular orientations. As shown in Fig. 4A, molecules of **4a** adopt an ordered parallel arrangement with a significant tilt angle of approximately 45°. Adjacent molecules exhibit a close

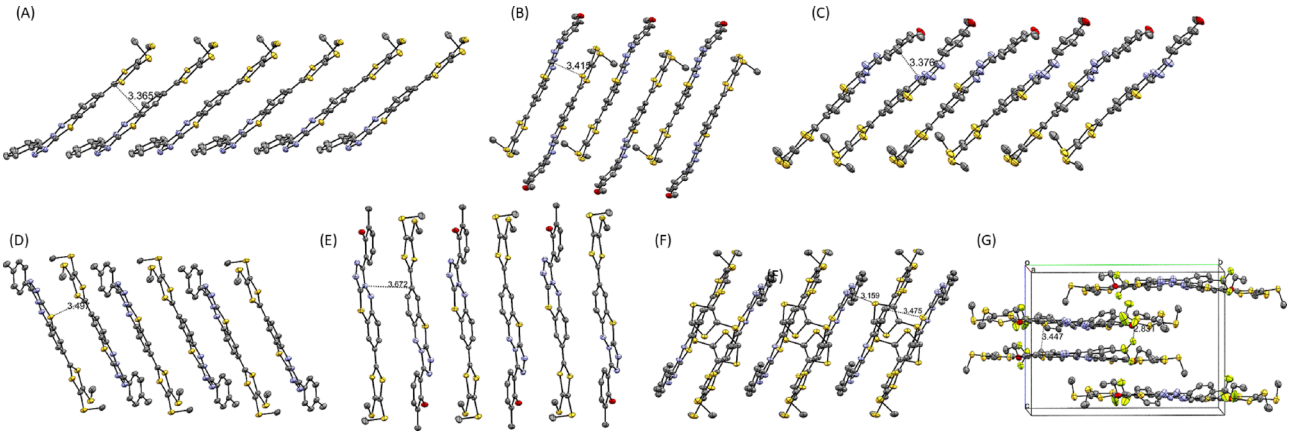

Fig. 4 Various π-stacking modes observed in the crystal structures of (A) **4a**, (B) **4b**, (C) [**4b** + H^+][CF_3COO^-], (D) **4c**, (E) **4h**, (F) **5c**, and (G) **6**. Selected interatomic distances are indicated in Å and hydrogen atoms are omitted for clarity.

C···C contact of 3.37 Å, indicative of efficient π-stacking. In contrast, compound **4b** crystallizes in an antiparallel arrangement (Fig. 4B), where neighboring molecules engage through intermolecular C···S contacts at a distance of 3.41 Å. Interestingly, protonation of **4b** with TFA switches the π-stacking mode to a parallel orientation (Fig. 4C). Similar to **4a**, the [**4b** + H]$^+$ cations pack in parallel with a tilt angle of 45°, exhibiting intimate intermolecular C···C contacts of 3.38 Å.

The tolyl-substituted derivative **4c** also packs in an antiparallel fashion, but with a relatively small tilt angle of approximately 20° (Fig. 4D). Its molecules form a slipped π-stack, characterized by intermolecular C···S contacts at a distance of 3.50 Å. In contrast, compound **4h** adopts an antiparallel packing mode with a very small tilt angle (Fig. 4E). The intermolecular separation between adjacent molecules ranges from 3.7 to 3.8 Å. This distance is slightly greater than the van der Waals diameter of carbon, indicating a relatively loose face-to-face π-stacking interaction.

Compound **5c** exhibits antiparallel π-stacking with a tilt angle of approximately 32° (Fig. 4F). The attachment of a dithiole ring to the edge of the planar π-framework does not disrupt face-to-face π-stacking. Instead, the dithiole ring facilitates the ordered packing by engaging in an intermolecular N···S contact (3.15 Å) between one of its sulfur atoms and a triazolyl nitrogen atom on an adjacent molecule. Furthermore, within the planar π-framework, a sulfur atom of the thiadiazine unit interacts with a benzo carbon of a neighboring molecule at a distance of 4.37 Å.

In contrast to the other derivatives, the crystal structure of **6** lacks the extended π-stacks described above. Instead, its unit cell contains a discrete π-dimer, where a pair of molecules adopt a parallel, face-to-face arrangement (Fig. 4G). Within this dimer, adjacent molecules exhibit a close F···F contact (2.83 Å) and an intimate C···S interaction (3.45 Å). The distinct packing behavior of **6** likely stems from the electron-withdrawing effect of its CF_3 substituent. Collectively, the diverse π-stacking motifs observed in these single-crystal structures demonstrate that the phenyl substituent on the **DTF-BTTD** π-framework serves as a handle for the bottom-up control of crystal packing. A deeper understanding of these substituent effects is valuable for the crystal engineering of **DTF-BTTD**-based organic electronic materials.

Electronic absorption properties of DTF-BTTD chromophores

The electronic absorption properties of the synthesized **DTF-BTTD** chromophores **4a–h** were investigated using UV-Vis spectroscopy and time-dependent density functional theory (TD-DFT) calculations. Their UV-Vis absorption spectra in CH_2Cl_2 at room temperature are shown in Fig. 5A and detailed absorption data are summarized in Table S1, SI. All compounds exhibit a similar broad absorption band between 450 and 650 nm. The strong absorbance in this visible region accounts for the purple color of their solutions. It is noteworthy that the molar absorptivities (ε) of our **DTF-BTTD** chromophores **4a–h** exceed 10^6 M^{-1} cm^{-1} in terms of their low-energy absorption bands. For context, this value significantly surpasses those of typical Ru-based DSSC sensitizers such as N719 dye ($\varepsilon \approx 1.42 \times 10^4$ M^{-1} cm^{-1} at 534 nm)[59] and conventional triphenylamine-based organic push–pull dyes (2–5 × 10^4 M^{-1} cm^{-1}),[60] and is greater than the established high-absorptivity dye classes including squaraines (1–3 × 10^5 M^{-1} cm^{-1})[61] and cyanines (1–2.5 × 10^5 M^{-1} cm^{-1}).[62] The combination of broad visible-region coverage (450–650 nm) and exceptionally high absorptivity makes the **DTF-BTTD** scaffold a promising candidate for light-harvesting applications requiring thin active layers.

To understand the origin of this low-energy band, TD-DFT calculations were performed on compound **4c** as a representative model. The simulated spectrum (*in vacuo*) predicts the lowest-energy absorption at 451 nm, arising primarily from a HOMO → LUMO transition (98% contribution) (Fig. 5B). As shown in Fig. 5C, both the HOMO and LUMO of **4c** are π-orbitals delocalized across the **DTF** and **BTTD** moieties, with negligible contribution from the tolyl substituent. The near-identical experimental low-energy bands for **4a–h** confirm that the appended phenyl group has little influence on these frontier orbitals. According to the TD-DFT calculation, the

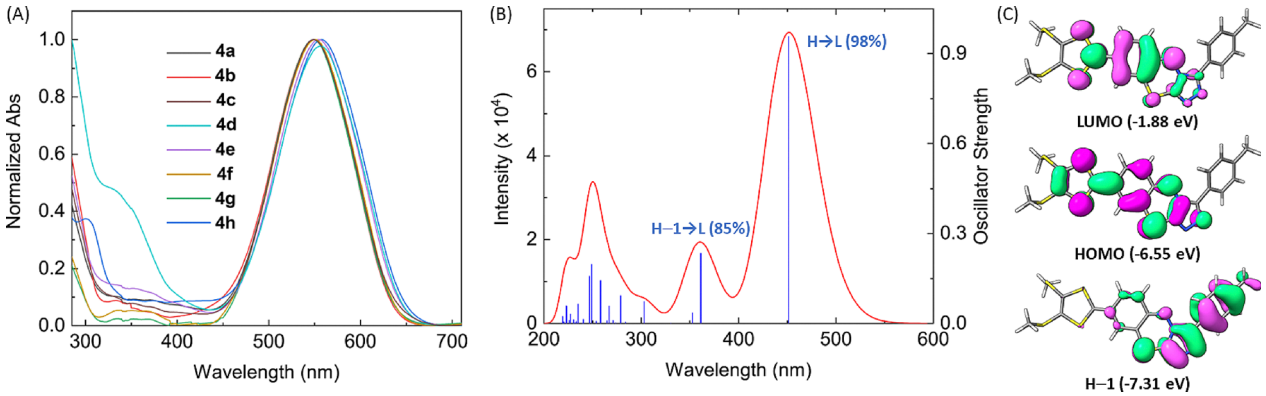

Fig. 5 (A) Normalized UV-Vis absorption spectra of **DTF-BTTD**s **4a–h** measured in CH_2Cl_2 at room temperature. (B) TD-DFT simulated UV-Vis spectrum of **4c** calculated at CAM-B3LYP/6-311+G(2d,p)//M06-2X/6-31+G(d,p) level of theory. (C) Plots of the frontier molecular orbitals (isovalue = 0.03 au) of **4c** that contribute to the low-energy absorption bands in its UV-Vis spectrum.

second lowest-energy absorption for **4c** appears at 361 nm and originates mainly from a H−1 → LUMO transition (85% contribution). The H−1 orbital is localized predominantly on the triazole and tolyl groups (Fig. 5C). This indicates that the appended phenyl group in **4a–h** can effectively modulate absorption in the higher-energy spectral region (*ca.* 300–400 nm). Overall, the TD-DFT simulated spectrum of **4c** agrees well with the experimental data in terms of the relative positions and intensities of the major absorption bands.

Our DFT calculations indicate that the HOMO → LUMO transition has strong intramolecular charge-transfer (ICT) character, suggesting that the **DTF-BTTD** compounds should exhibit solvatochromism.[63,64] To investigate this, the UV-Vis absorption spectra of compound **4c** were measured in various organic solvents (Fig. 6A). The results confirm that the low-energy absorption maximum is solvent-dependent.

To quantify the solvatochromic effect, the transition energies (E_{abs}) were correlated with the $E_T(30)$ solvent polarity scale.[64] The $E_T(30)$ scale was chosen for its broad parameter set and sensitivity to both specific and non-specific solvent interactions. As shown in Fig. 6B, two distinct linear correlations are observed. The first correlation includes hexane, diethyl ether, ethyl acetate, acetonitrile, isopropanol, and ethanol. The second includes toluene, THF, chloroform, DMF, and DMSO. The result for methanol is an outlier and does not fit either trend. In general, more polar solvents induce a greater redshift in the absorption maximum. The origin of the two linear correlations is not yet clear and requires further study; however, their existence suggests two distinct solvation modes for **4c** in different organic media. Given that one group consists primarily of oxygenated solvents, specific interactions such as hydrogen bonding or O···N and O···S contacts may contribute significantly to the solvatochromic shifts, in addition to general solvent polarity effects.

X-ray analysis confirmed that the **DTF-BTTD** structure can be protonated by TFA at the triazolyl unit to form a stable salt. We therefore anticipated that the **DTF-BTTD** system would exhibit acidochromism in solution. To investigate this, UV-Vis titrations of **4c** with TFA were performed (Fig. 7).

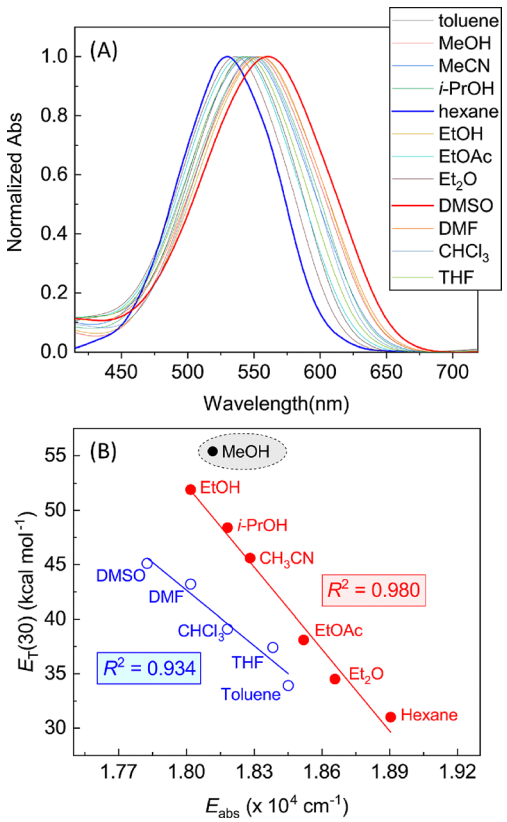

Fig. 6 (A) UV-Vis absorption spectra of **4c** measured in different organic solvents. (B) Correlation plots of maximum absorption energy (E_{abs}) against the solvent scale $E_T(30)$.

The titration revealed two distinct stages of spectral change in the long-wavelength region. In the first stage (0.0 to 43.1 molar equivalents of TFA), the low-energy absorption band at 549 nm gradually shifted to 578 nm, with a slight increase in intensity (Fig. 7A). In the second stage (up to 234.7 molar equivalents), this band continued to redshift, and a shoulder at 634 nm gradually emerged (Fig. 7B). The enhancement, rather than attenuation, of absorbance upon protonation

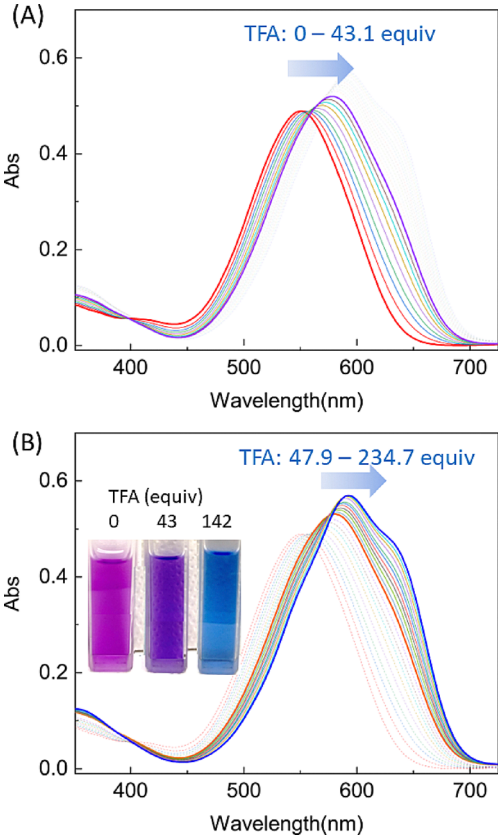

Fig. 7 UV-Vis spectral analysis monitoring the titration of **4c** (5.08×10^{-5} M in CH_2Cl_2) with TFA: (A) addition of TFA from 0.0 to 43.1 mole equiv., and (B) addition of TFA from 47.9 to 234.7 mole equiv. Arrows indicate the trend of spectral change with increasing TFA addition. Inset: Photographic image of the solutions of **4c** with varying amounts of TFA.

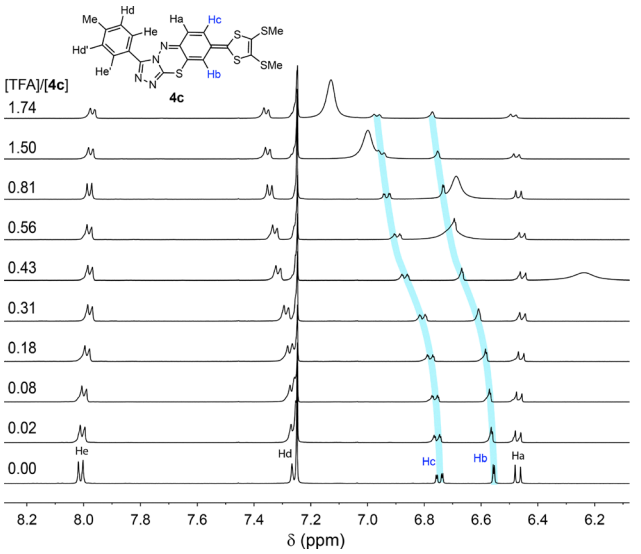

Fig. 8 ^{1}H NMR (300 MHz, $CDCl_3$) spectra monitoring the titration of **4c** (3.18×10^{-3} M) with TFA at room temperature. The cyan curves highlight the shifts of Hb and Hc during titration.

demonstrates excellent acid tolerance. The two distinct spectral stages suggest that **4c** undergoes consecutive protonation to form mono- and diprotonated species. Based on the X-ray structure of [**4b** + H^+][CF_3COO^-], the first protonation likely occurs at the N3 position of the triazolyl unit. The site of the second protonation remains unclear. Overall, protonation of the **DTF-BTTD** framework strengthens the donor–acceptor interaction between the **DTF** and **BTTD** units, resulting in a redshifted and intensified absorption in the visible region.

To probe the solution-phase properties of protonated **DTF-BTTD**, a ^{1}H NMR titration of **4c** was performed in $CDCl_3$ (Fig. 8). During the titration, two benzo protons of the **BTTD** unit (Hb and Hc) shifted significantly downfield, while the third benzo proton (Ha) remained largely unaffected. This result confirms that protonation occurs predominantly at the triazolyl group. Protonation at this site significantly reduces the electron density at the carbon atoms bearing Hb and Hc through conjugation, explaining their pronounced downfield shifts. Protonation at the thiadiazine ring can be ruled out, as this would be expected to cause a more substantial shift in the Ha signal. The NMR data further indicate that the benzo unit becomes more electron-deficient upon protonation, thereby enhancing its donor–acceptor interaction with the **DTF** group. This interpretation is consistent with the redshift observed in the UV-Vis titration experiment.

Electrochemical properties of DTF-BTTD chromophores

To characterize the redox properties of the **DTF-BTTD** framework, cyclic voltammetry (CV) was first performed on compound **4a**. The phenyl appendage in **4a** exerts minimal electronic influence on the core **DTF-BTTD** π-system; therefore, its CV response primarily reflects the intrinsic redox activity of the **DTF-BTTD** unit.

The CV profiles of **4a** in the positive and negative potential windows are shown in Fig. 9A and B, respectively. In the positive window, the first anodic scan exhibits a well-defined oxidation peak at +1.01 V, which is reasonably assigned to the one-electron oxidation of the **DTF** moiety to form a radical cation. The subsequent cathodic scan shows a significant reduction peak at +0.97 V. This reduction peak is attributed to a species generated by a follow-up chemical reaction of the initially formed radical cation. This interpretation is supported by the evolution of the voltammogram in subsequent cycles: the original oxidation peak at +1.01 V disappears, and a new anodic peak emerges at +1.44 V in the second and third scans.

In contrast to **4a**, the voltammograms of **5a** do not exhibit the characteristic features of an EC (electrochemical-chemical) process. This difference in reactivity is likely due to the structural modification in **5a**, where the site β to the **DTF** group is incorporated into a dithiole ring. As shown in Fig. 9C, the first anodic scan displays two oxidation peaks at +1.14 V and +1.62 V, assigned to the sequential one-electron oxidations of the **DTF** and dithiole groups, respectively. In subsequent cycles, the first peak (**DTF** oxidation) disappears, while the second peak (dithiole oxidation) persists. No significant reduction peaks are observed in the corresponding cathodic scans. This irreversible electrochemical behavior suggests that facile

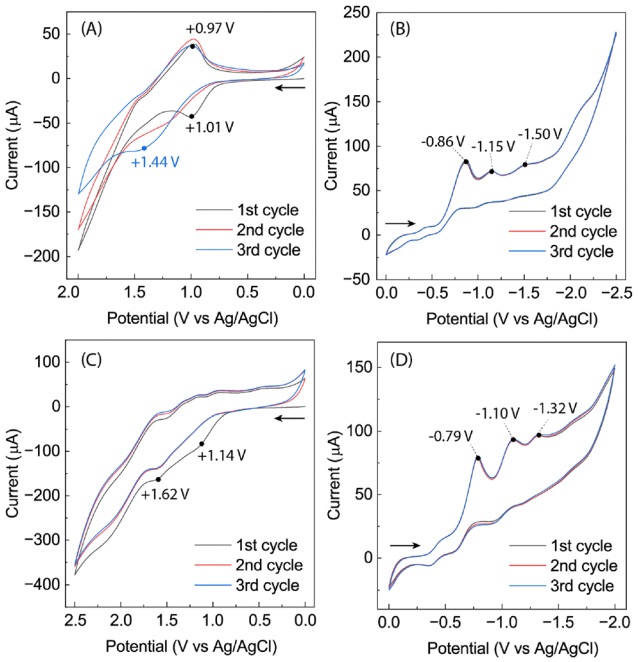

Fig. 9 Cyclic voltammograms of compound **4a** scanned in (A) the positive and (B) negative potential windows, respectively. Cyclic voltammograms of compound **5a** scanned in (C) the positive and (D) negative potential windows, respectively. CV experimental conditions: Bu_4NPF_6 (0.1 M) as the electrolyte, glassy carbon as the working electrode, Ag/AgCl as the reference electrode, Pt wire as the counter electrode, CH_2Cl_2 as the solvent, and scan rate = 0.20 V s^{-1}. Arrows indicate the directions of initial scans.

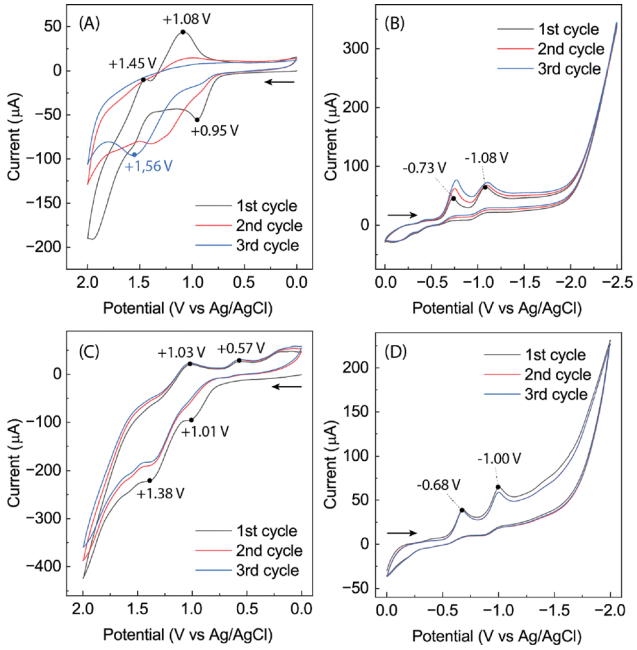

Fig. 10 Cyclic voltammograms of compound **4b** scanned in (A) the positive and (B) negative potential windows, respectively. Cyclic voltammograms of compound **4c** scanned in (C) the positive and (D) negative potential windows, respectively. CV experimental conditions: Bu_4NPF_6 (0.1 M) as the electrolyte, glassy carbon as the working electrode, Ag/AgCl as the reference electrode, Pt wire as the counter electrode, CH_2Cl_2 as the solvent, and scan rate = 0.20 V s^{-1}. Arrows indicate the directions of initial scans.

chemical reactions follow the initial oxidation of the **DTF** moiety. A detailed mechanistic understanding of these redox pathways will require further investigation.

In the negative potential window, the cyclic voltammograms of **4a** exhibit three irreversible reduction peaks at −0.86 V, −1.15 V, and −1.50 V (Fig. 9B). In contrast to the behavior in the positive window, these voltammograms remain unchanged over multiple scan cycles. The three peaks are assigned to sequential one-electron reductions of the **BTTD** unit. Similar reduction patterns are observed for **5a**, although the peak potentials are slightly shifted relative to those of **4a**.

To investigate the substituent effects of the appended phenyl group on the redox activity of **DTF-BTTD** derivatives, we selected compounds **4b** and **4d** for CV analysis. These compounds feature a strong electron-donating group (OMe) and an electron-withdrawing group (CF_3), respectively, on the phenyl ring. The cyclic voltammogram of **4b** in the positive potential window (Fig. 10A) exhibits significant EC features similar to those of **4a**. The first anodic scan shows a distinct oxidation peak at +0.95 V. The corresponding reverse scan reveals two reduction peaks at +1.45 V and +1.08 V. By the third cycle, the initial oxidation peak at +0.95 V has nearly vanished, and a new oxidation peak is clearly present at +1.56 V. In contrast to **4a**, the cathodic peaks in the reverse scans of **4b** also diminish progressively. This behavior suggests that the oxidized product(s) of **4b** undergo further chemical reactions, likely involving the activated anisole group, leading to irreversible electrochemical features.

The CF_3-substituted derivative **4d** exhibits markedly different voltammetric behavior in the positive potential window (Fig. 10C). The first cycle shows two oxidation peaks at +1.01 V and +1.38 V, with corresponding reduction peaks at +0.57 V and +1.03 V. In subsequent cycles, the first oxidation peak (+1.01 V) disappears, while the other peaks persist. Although a detailed electrochemical mechanism remains unclear, these results clearly demonstrate that the substituent on the phenyl ring of the **DTF-BTTD** framework can significantly modulate its redox activity in the positive potential window.

In the negative potential window, both **4b** and **4d** exhibit similar irreversible reduction profiles, with two cathodic peaks at −0.73 V and −1.08 V for **4b** and −0.68 V and −1.00 V for **4d**. The potentials for the electron-donating derivative **4b** are slightly shifted cathodically relative to those for the electron-withdrawing derivative **4d**, indicating that the appended phenyl group exerts only a weak influence on the reduction potentials. In summary, the electrochemical redox properties of **DTF-BTTD** derivatives are highly sensitive to repeated scanning in the positive potential window. In contrast, the reduction features in the negative window show minimal variation. Detailed CV data for the remaining **DTF-BTTD** derivatives are provided in the SI (Fig. S31–S35).

The cyclic voltammograms measured in the positive and negative potential windows were used to determine the

Table 2 Summary of the first oxidation and reduction potentials (in V) and electrochemical band gaps (E_g, in eV) for **4a–h**

Entry	E^1_{ox}	E^1_{red}	E_g
4a	+0.773	−0.619	1.392
4b	+0.771	−0.606	1.377
4c	+0.756	−0.597	1.353
4d	+0.779	−0.556	1.335
4e	+0.740	−0.575	1.315
4f	+0.728	−0.688	1.416
4g	+0.780	−0.594	1.374
4h	+0.781	−0.588	1.369

electrochemical band gaps (E_g) of these compounds. The E_g was calculated as the difference between the onset potential of the first oxidation (E^1_{ox}) and the onset potential of the first reduction (E^1_{red}) from the first CV cycle. As listed in Table 2, the **DTF-BTTD** compounds **4a–h** exhibit band gaps ranging from 1.315 eV to 1.416 eV. This narrow range indicates that attaching various substituents to the phenyl group only slightly adjusts the band gaps, which is consistent with the relatively weak substitution effects observed in the UV-Vis analysis. This behavior reflects a limited ability to tune the electronic band gaps of the **DTF-BTTD** chromophores by modifying the phenyl appendage. Conversely, it suggests that the **DTF-BTTD** chromophores are tolerant to structural modifications such as the attachment of anchoring groups for surface functionalization or the addition of synthetic handles for structural extension without significantly disrupting their core electronic properties.

Covalent functionalization of TiO_2 nanoparticles with 4c

Having elucidated the fundamental properties of the **DTF-BTTD** compounds, we next explored their applicability in materials science. Organic dyes with strong visible to near-infrared (Vis-NIR) absorption are extensively used in dye-sensitized solar cells and photocatalytic systems.[8,28,65–67] A particularly common strategy for generating new functional composites involves combining such dyes with inorganic semiconductor nanoparticles, such as titanium dioxide (TiO_2).[68]

Effective immobilization of an organic dye on a metal oxide surface typically requires an anchoring group, such as a carboxylic acid or cyanoacrylic acid group. The **DTF-BTTD** molecular structure contains multiple heteroatoms that can potentially act as ligand sites for binding to transition metals. We therefore hypothesized that **DTF-BTTD** compounds might exhibit sufficient affinity for metal oxide surfaces to form dye-functionalized hybrid materials. To test this, we performed IR analysis on mixtures of anatase TiO_2 nanoparticles with compound **4c**. In our experiments, TiO_2 nanoparticles were first dispersed in ethanol to form a suspension, to which different amounts of **4c** were added. The resulting mixtures were dried and analyzed by IR spectroscopy. As shown in Fig. 11, pristine TiO_2 nanoparticles exhibit a broad band at 1638 cm^{-1}, assigned to the O–H bending mode of adsorbed surface water.[69–71] When mixed with a small amount of **4c**, this water O–H bending peak disappears. The IR spectrum of this mixture is drastically different from the spectra of pristine TiO_2 and **4c**, indicating

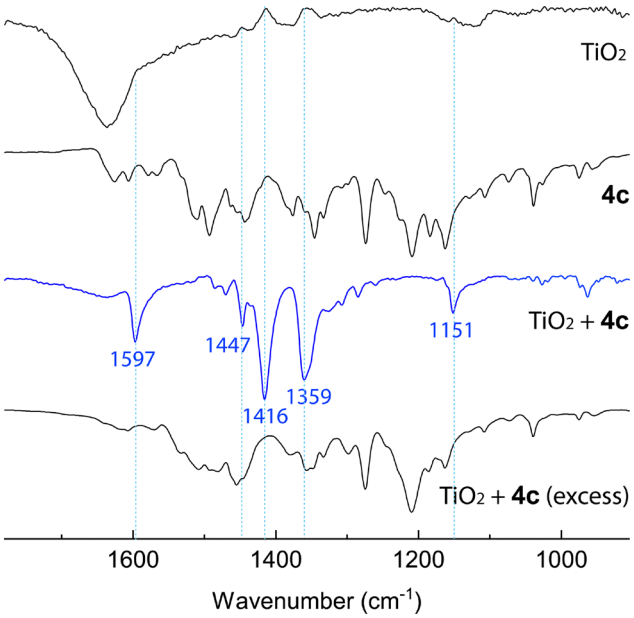

Fig. 11 FTIR spectra of TiO_2 nanoparticles, compound **4c**, and their mixtures.

covalent functionalization of the TiO_2 nanoparticle surface by **4c**. In contrast, when TiO_2 nanoparticles were mixed with an excess of **4c**, the observed IR modes resemble those of pure **4c**, suggesting the **4c**/TiO_2 hybrids were fully encapsulated by **4c** molecules *via* non-covalent interactions.

To better understand the covalent interactions between **4c** and TiO_2 nanoparticles, we computationally modeled a simplified system consisting of a **4c** molecule and a $(TiO_2)_{15}$ cluster. We first searched for stable structures of this assembly using the CREST (conformer-rotamer ensemble sampling tool) program.[72–74] The most stable conformer identified by CREST was then subjected to geometry optimization using density functional theory (DFT) calculations with the Gaussian 16 software package.[75] Fig. 12A shows the optimized structure of the **4c**–$(TiO_2)_{15}$ complex. One of the triazolyl nitrogen atoms forms a Ti–N bond with a length of 2.06 Å. This metallation site is consistent with the preferred protonation site observed in X-ray analysis, indicating that this specific triazole nitrogen is the most active ligand for interacting with Ti. The formation of the Ti–N bond causes significant elongation of a nearby Ti–O bond to 3.35 Å (see the dashed bond in Fig. 12A). The weakening of this Ti–O bond allows the oxygen atom to form a Ti═O double bond (1.63 Å), which is much shorter than the other Ti–O bonds in the cluster. In addition to this covalent Ti–N bond, the **DTF-BTTD** segment of **4c** is notably bent, enabling the edge of **4c** to form S···O and H···O interactions with the TiO_2 cluster.

Fig. 12B compares the calculated IR spectra of pristine **4c** and the **4c**–$(TiO_2)_{15}$ complex. In the 1100–1700 cm^{-1} region, **4c** is predicted to exhibit three significant vibrational bands at 1641, 1476, and 1370 cm^{-1}. The band at 1641 cm^{-1} is assigned to C═C stretching in the benzo unit, while the bands at 1476 and 1370 cm^{-1} correspond to C═N stretching modes in the triazole and dithiazine units, respectively. The experimental

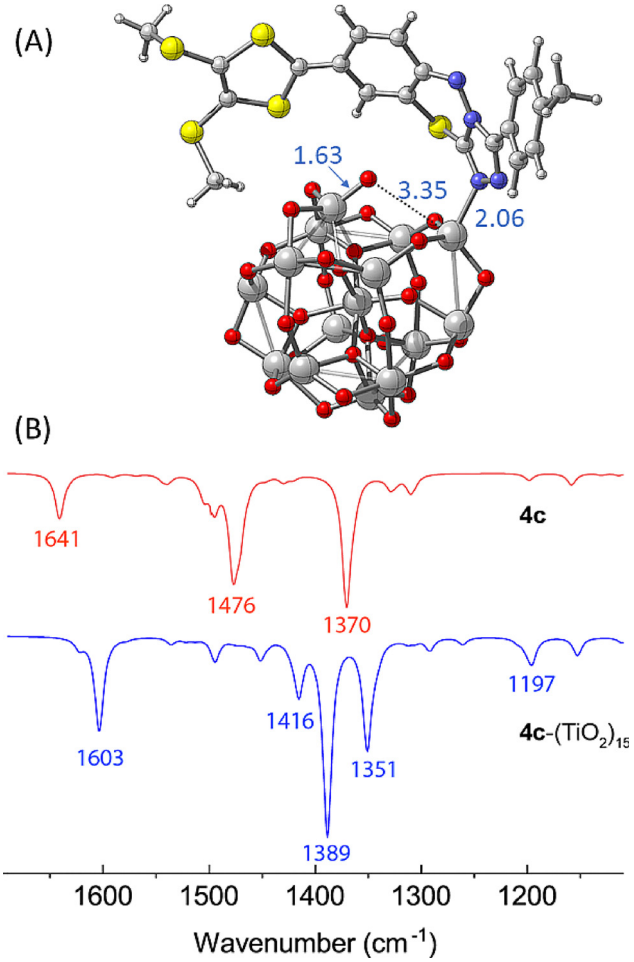

Fig. 12 (A) Optimized geometry of the complex of **4c** and a $(TiO_2)_{15}$ cluster. Selected interatomic distances are highlighted in Å. (B) DFT-simulated IR spectra of **4c** (red trace) and the complex of **4c** and $(TiO_2)_{15}$ (blue trace). Calculations were done at the B3LYP-D3/6-31G(d)/LanL2DZ level of theory with a scaling factor of 0.97.

spectrum of **4c** is more complex, likely due to the presence of multiple conformers and aggregates in the solid sample. For the **4c**–$(TiO_2)_{15}$ complex, five significant vibrational bands are predicted in this region. These show excellent agreement with the experimental IR spectrum of the **4c**/TiO_2 nanoparticle mixture (highlighted bands in Fig. 11), validating our computational model for simulating the surface interactions. The DFT calculations indicate that upon covalent bonding to the TiO_2 cluster, the benzo C=C stretching vibration shifts to a lower frequency (1603 cm^{-1}), consistent with the experimental trend. Three peaks predicted at 1416, 1389, and 1351 cm^{-1} are assigned to C=N vibrations of **4c**. In the experimental spectrum, corresponding peaks are clearly observed at 1447, 1416, and 1359 cm^{-1}, showing very good agreement. Notably, the unique Ti=O bond in the complex is predicted to vibrate at 1197 cm^{-1}. A characteristic band appears in the experimental spectrum at 1151 cm^{-1}, providing strong evidence for covalent interaction between **4c** and TiO_2. This assignment is supported by a previous literature report on Ti=O vibrational properties.[76]

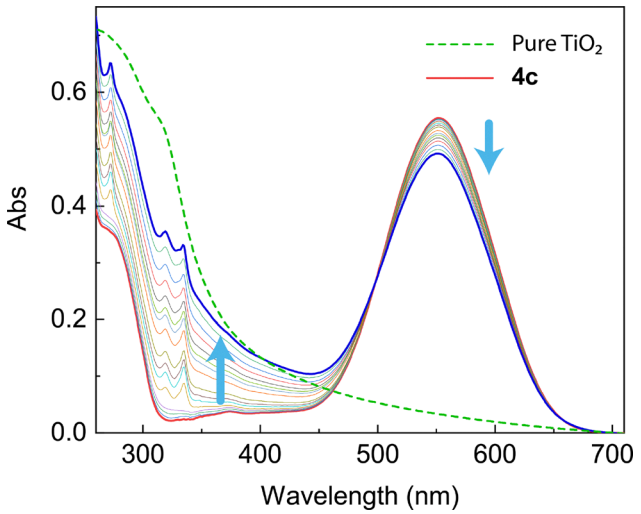

Fig. 13 UV-Vis spectral analysis monitoring the titration of **4c** (1.05×10^{-5} M in EtOH) with TiO_2 nanoparticles from 0.00 to 4.22 mole equiv. Arrows indicate the trend of spectral changes with the progress of the titration. The trace depicted by the dashed line is the UV-Vis absorption spectrum of TiO_2 nanoparticles suspended in EtOH.

Following the IR analysis, we examined the UV-Vis absorption properties of **4c**-functionalized TiO_2 nanoparticles *via* a titration experiment. As shown in Fig. 13, incremental additions of TiO_2 nanoparticles were made to a solution of **4c** in ethanol. During the titration, the broad visible absorption band of **4c** (*ca.* 450–680 nm) showed only slight attenuation. In contrast, the absorbance in the UV region (300–450 nm) increased significantly due to the intrinsic absorption of TiO_2. Furthermore, three relatively sharp absorption bands emerged at 335, 319, and 272 nm, providing additional evidence for covalent interactions between **4c** and the TiO_2 nanoparticles. Overall, the UV-Vis study indicates that surface functionalization of TiO_2 nanoparticles with **4c** yields a hybrid material capable of absorbing a broad spectrum of light. This enhanced absorption profile is beneficial for applications in photovoltaics and visible-light-promoted photocatalysis.

Finally, we examined the effect of surface functionalization with **4c** on the size of TiO_2 nanoparticles. Various amounts of **4c** were added to a suspension of TiO_2 nanoparticles in ethanol, and the particle size distributions of the resulting mixtures were measured by dynamic light scattering (DLS). As shown in Fig. 14, the pristine TiO_2 nanoparticles have diameters ranging from *ca.* 50 to 500 nm. The addition of **4c** caused only minor changes in the size distribution. While a small fraction of particles increased in size to 500–600 nm, the majority remained within the original 50–500 nm range. These DLS results suggest that **4c** forms only a monolayer or a few layers on the TiO_2 surface and that the functionalization does not induce significant interparticle aggregation.

In summary, our investigation into the interactions between **4c** and TiO_2 nanoparticles demonstrates their significant potential for use in optoelectronic devices, particularly dye-sensitized solar cells (DSSCs). The **DTF-BTTD** chromophores

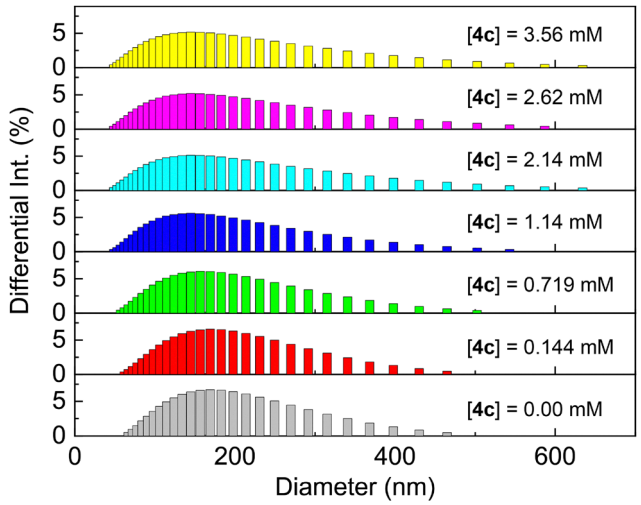

Fig. 14 DLS analysis showing the particle size distributions for anatase TiO_2 nanoparticles (7.50 mg L^{-1}) mixed with various amounts of **4c**.

exhibit several advantageous properties: (1) remarkably high molar absorptivity (exceeding 10^5 M^{-1} cm^{-1}; see Table S1, SI) in the visible region, enabling strong light harvesting; (2) relatively small band gaps (Table 2), which facilitate broader spectral coverage; (3) a triazolyl unit that acts as an effective anchoring group, promoting direct interaction between the dye's π-conjugated framework and the TiO_2 surface, likely enhancing electron injection efficiency; and (4) minimal aggregation on the TiO_2 surface, as shown by DLS, a factor known to improve DSSC performance by reducing intermolecular energy transfer and charge recombination. This combination of properties positions these dyes as promising candidates for achieving enhanced power conversion efficiencies in DSSCs, warranting further experimental exploration.

Tests of antibacterial activities

The global spread of bacterial drug resistance necessitates the discovery of new and potent antimicrobial agents.[77–79] Heterocyclic compounds containing a triazole ring are of particular interest due to their broad bioactivities, including antibacterial and antifungal properties.[80–83] Our synthesized **DTF-BTTD** chromophores incorporate a 1,2,4-triazole ring fused to a benzothiadiazine framework. As 1,2,4-triazole is a well-known pharmacophore with many derivatives exhibiting antibacterial activity,[80,82] we evaluated the antibacterial properties of **4c** against representative Gram-negative (*Escherichia coli*) and Gram-positive (*Staphylococcus aureus*) bacteria. While we did not design these chromophores *de novo* as antibacterial agents following certain established molecular guidelines, the well-known pharmacophoric nature of the 1,2,4-triazole motif prompted us to explore whether this structural feature might impart additional functionality. Fortuitously, we discovered that compound **4c** exhibited notable antibacterial activity against these two representative bacteria. We therefore present this antibacterial property as an unexpected, yet valuable, multifunctional attribute of our chromophores.

Table 3 Results of inhibition zones of various test solutions against two bacterial strains measured by the filter paper disc diffusion method

Entry	Concentration (mM)	Zone of Inhibition (mm)	
		E. coli	*S. aureus*
4c	2.5	17.8 ± 0.4	15.7 ± 0.3
	0.5	14.0 ± 0.4	13.3 ± 0.5
	0.1	12.1 ± 0.5	12.2 ± 0.4
2i	2.5	14.3 ± 0.4	12.2 ± 0.5
	0.5	13.7 ± 0.6	11.3 ± 0.4
	0.1	10.0 ± 0.3	9.9 ± 0.4

The disk diffusion method (DDM)[84] was used to assess the antibacterial performance of **4c** at various concentrations (Table 3). To probe the influence of the **DTF** functional group, we also tested the reference compound **2i**, a stable, nearly planar aryl-substituted **BTTD** (Fig. 15). A comparison of their activities reveals whether the **DTF** group enhances or attenuates bioactivity. As shown in Table 3, both **4c** and **2i** exhibited inhibitory activity against both bacteria at low concentrations (0.1–2.5 mM), with a stronger effect observed against *E. coli* than *S. aureus*. Notably, **4c** produced larger inhibition zones than **2i** under identical conditions, confirming that **DTF** functionalization enhances antibacterial performance.

Following the antibacterial assays, we explored the application of **4c** as a functional dye to impart self-cleaning properties to glass surfaces. Fluorine-doped tin oxide (FTO) glass was selected as the substrate due to its widespread use in optoelectronic devices (*e.g.*, solar cells, touchscreens, and smart windows). For such applications, maintaining surface transparency is critical, and bacterial adhesion is a common cause of surface fouling. We examined the attachment of two model bacteria, *E. coli* and *B. subtilis*, to four types of FTO substrates: (I) neat FTO, (II) FTO coated with **4c**, (III) FTO coated with TiO_2 particles, and (IV) FTO coated with both **4c** and TiO_2. Fig. 16 summarizes the results of these attachment tests after the substrates were immersed in bacterial cultures for 12 h under dark or ambient light conditions, while detailed experimental conditions and procedures are provided in the SI (see Fig. S37–S52).

As shown in Fig. 16A, the **4c**-coated FTO substrate exhibited the lowest *E. coli* attachment under dark conditions, consistent with the enhanced anti-*E. coli* activity of **4c** observed in prior antibacterial assays. Under ambient light, substrates coated with **4c** and TiO_2 showed significantly reduced *E. coli* attachment, indicating light-induced self-cleaning behavior. The best

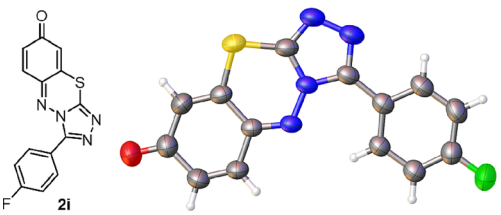

Fig. 15 Chemical structure (left) and ORTEP drawing (at 50% ellipsoid probability) of compound **2i**.

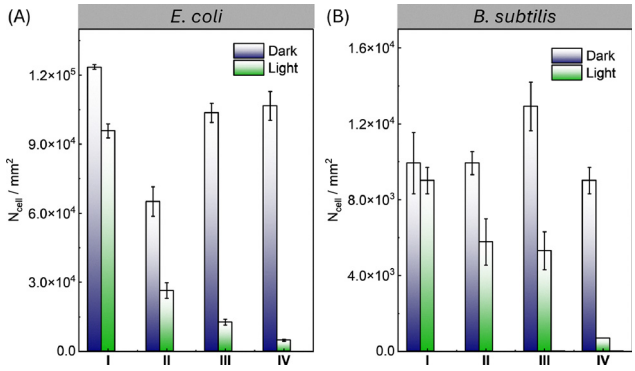

Fig. 16 Bacterial attachment assays on FTO glass substrates with (A) *E. coli* and (B) *B. subtilis*. Substrate conditions: I, neat; II, coated with **4c**; III, coated with TiO_2; IV, coated with **4c**-TiO_2. N_{cell} represents the number of bacteria counted within a defined square area on the surface.

bacterial resistance was observed for the surface coated with both **4c** and TiO_2, which retained the fewest *E. coli* cells after 12 h of immersion in the bacterial culture. This performance can be attributed to a synergistic effect between **4c** and TiO_2. Specifically, **4c** can be photoexcited by visible light, given its strong absorptivity in the visible spectral range, and subsequently transfer electrons to the TiO_2 surface, promoting the generation of bactericidal reactive oxygen species (ROS).[85]

In the *B. subtilis* tests (Fig. 16B), the four substrates exhibited similar levels of bacterial attachment under dark conditions, with the TiO_2-coated glass showing the highest bacterial density. This indicates that neither **4c** nor TiO_2 provides significant antibacterial activity against *B. subtilis* in the dark. Under ambient light, however, all coated substrates showed reduced bacterial attachment compared to the neat glass. Among these, the substrate coated with both **4c** and TiO_2 demonstrated the most pronounced resistance, highlighting a strong photo-induced synergistic effect. Collectively, these bacterial attachment results demonstrate that hybrids of the **DTF-BTTD** chromophore with TiO_2 can serve as antibacterial coatings that effectively protect optically transparent substrates from biofouling.

Conclusions

In summary, we have developed a new family of **DTF-BTTD** chromophores that exhibit strong visible-light absorption and versatile redox activities, driven by intramolecular push–pull effects across their extended π-conjugated frameworks. By modifying the aryl group attached to the triazolyl moiety, we can tune the molecular conformation, crystal packing, and electronic band gaps, establishing the **DTF-BTTD** system as a flexible molecular platform for advanced optoelectronic applications. The fused 1,2,4-triazole ring provides an active site for acid interaction, resulting in pronounced acidochromic effects. Protonation enhances and redshifts the visible-region absorption, making **DTF-BTTD** compounds robust organic dyes that retain strong visible-light absorptivity under acidic conditions. Electrochemical studies show that while these compounds exhibit consistent reduction behavior (indicating reliable acceptor performance), their oxidation properties vary significantly. For some derivatives, oxidation follows complex EC mechanisms, likely due to the reactivity of the generated **DTF** radical cation–a subject that merits further investigation. The triazole unit also functions as an effective ligand, binding to TiO_2 nanoparticle surfaces *via* covalent Ti–N linkages. This suggests promising applications in surface-functionalized metal oxides for devices such as dye-sensitized solar cells and photocatalytic systems. Furthermore, **DTF-BTTD** structures display enhanced antibacterial activity compared to their **BTTD** precursors, and hybrids of **DTF-BTTD** with TiO_2 demonstrate superior inhibition of bacterial attachment to glass surfaces under ambient light. These properties offer a novel light-powered self-cleaning mechanism for designing and fabricating multifunctional, regenerative, optically transparent surfaces.

Conflicts of interest

There are no conflicts to declare.

Data availability

The data supporting this article have been included as part of the supplementary information (SI). Supplementary information: detailed synthetic procedures, spectroscopic characterizations of new compounds, single-crystal X-ray crystallographic data, UV-Vis absorption, cyclic voltammetric data, and results of DFT calculations as well as antibacterial activity measurements. See DOI: **https://doi.org/10.1039/d6qm00098c**.

CCDC 2132937–2132944 contain the supplementary crystallographic data for this paper.[86a–h]

Acknowledgements

We acknowledge the funding support from the Natural Sciences and Engineering Research Council of Canada (NSERC) and the Canada Foundation for Innovation (CFI). FS and HF acknowledge the School of Graduate Studies (SGS), Memorial University of Newfoundland for providing a graduate scholarship. KN thanks the Zhejiang Provincial Natural Science Foundation of China for funding support (Grant no. LTGS24B070001). Dr. Jian-bin Lin at C-CART, Memorial University of Newfoundland is acknowledged for collecting the single-crystal crystallographic data and solving the X-ray structures reported in this work. The Digital Research Alliance of Canada (the Alliance) and ACENET are acknowledged for providing computational resources.

References

1 H. Zollinger, *Color chemistry: syntheses, properties, and applications of organic dyes and pigments*, John Wiley & Sons, 2003.

2 W. Herbst and K. Hunger, *Industrial organic pigments: production, properties, applications*, John Wiley & Sons, 2006.
3 M. Gsänger, D. Bialas, L. Huang, M. Stolte and F. Würthner, Organic semiconductors based on dyes and color pigments, *Adv. Mater.*, 2016, **28**, 3615–3645.
4 W. Cheng, H. Chen, C. Liu, C. Ji, G. Ma and M. Yin, Functional organic dyes for health-related applications, *View*, 2020, **1**, 20200055.
5 M. Saleem, M. Rafiq, M. Hanif, M. A. Shaheen and S.-Y. Seo, A brief review on fluorescent copper sensor based on conjugated organic dyes, *J. Fluoresc.*, 2018, **28**, 97–165.
6 E. Oliveira, E. Bértolo, C. Núñez, V. Pilla, H. M. Santos, J. Fernández-Lodeiro, A. Fernández-Lodeiro, J. Djafari, J. L. Capelo and C. Lodeiro, Green and red fluorescent dyes for translational applications in imaging and sensing analytes: A dual-color flag, *ChemistryOpen*, 2018, **7**, 9–52.
7 Z. Jin, W. Yim, M. Retout, E. Housel, W. Zhong, J. Zhou, M. S. Strano and J. V. Jokerst, Colorimetric sensing for translational applications: from colorants to mechanisms, *Chem. Soc. Rev.*, 2024, **53**, 7681–7741.
8 Y. Ooyama and Y. Harima, Molecular designs and syntheses of organic dyes for dye-sensitized solar cells, *Eur. J. Org. Chem.*, 2009, 2903–2934.
9 M. Liang and J. Chen, Arylamine organic dyes for dye-sensitized solar cells, *Chem. Soc. Rev.*, 2013, **42**, 3453–3488.
10 J. Wang, K. Liu, L. Ma and X. Zhan, Triarylamine: Versatile platform for organic, dye-sensitized, and perovskite solar cells, *Chem. Rev.*, 2016, **116**, 14675–14725.
11 H. Mustroph, M. Stollenwerk and V. Bressau, Current developments in optical data storage with organic dyes, *Angew. Chem., Int. Ed.*, 2006, **45**, 2016–2035.
12 S. Fukuzumi and K. Ohkubo, Organic synthetic transformations using organic dyes as photoredox catalysts, *Org. Biomol. Chem.*, 2014, **12**, 6059–6071.
13 S. G. Amos, M. Garreau, L. Buzzetti and J. Waser, Photocatalysis with organic dyes: Facile access to reactive intermediates for synthesis, *Beil. J. Org. Chem.*, 2020, **16**, 1163–1187.
14 M. Forchetta, F. Valentini, V. Conte, P. Galloni and F. Sabuzi, Photocatalyzed oxygenation reactions with organic dyes: State of the art and future perspectives, *Catalysts*, 2023, **13**, 220.
15 P.-T. Chou and Y. Chi, Phosphorescent dyes for organic light-emitting diodes, *Chem. – Eur. J.*, 2007, **13**, 380–395.
16 K.-H. Kim and J.-J. Kim, Origin and control of orientation of phosphorescent and TADF dyes for high-efficiency OLEDs, *Adv. Mater.*, 2018, **30**, 1705600.
17 J. Tagare and S. Vaidyanathan, Recent development of phenanthroimidazole-based fluorophores for blue organic light-emitting diodes (OLEDs): An overview, *J. Mater. Chem. C*, 2018, **6**, 10138–10173.
18 L. Torsi, M. Magliulo, K. Manoli and G. Palazzo, Organic field-effect transistor sensors: A tutorial review, *Chem. Soc. Rev.*, 2013, **42**, 8612–8628.
19 S. Yuvaraja, A. Nawaz, Q. Liu, D. Dubal, S. G. Surya, K. N. Salama and P. Sonar, Organic field-effect transistor-based flexible sensors, *Chem. Soc. Rev.*, 2020, **49**, 3423–3460.
20 Y. Cai, W. Si, W. Huang, P. Chen, J. Shao and X. Dong, Organic dye based nanoparticles for cancer phototheranostics, *Small*, 2018, **14**, 1704247.
21 B. Zhou, Y. Li, G. Niu, M. Lan, Q. Jia and Q. Liang, Near-infrared organic dye-based nanoagent for the photothermal therapy of cancer, *ACS Appl. Mater. Interface*, 2016, **8**, 29899–29905.
22 C. Yin, X. Li, Y. Wang, Y. Liang, S. Zhou, P. Zhao, C.-S. Lee, Q. Fan and W. Huang, Organic semiconducting macromolecular dyes for NIR-II photoacoustic imaging and photothermal therapy, *Adv. Funct. Mater.*, 2021, **31**, 2104650.
23 S. Luo, E. Zhang, Y. Su, T. Cheng and C. Shi, A review of NIR dyes in cancer targeting and imaging, *Biomaterial*, 2011, **32**, 7127–7138.
24 J. Wu, Z. Shi, L. Zhu, J. Li, X. Han, M. Xu, S. Hao, Y. Fan, T. Shao, H. Bai, B. Peng, W. Hu, X. Liu, C. Yao, L. Li and W. Huang, The design and bioimaging applications of NIR fluorescent organic dyes with high brightness, *Adv. Opt. Mater.*, 2022, **10**, 2102514.
25 H. Meier, Conjugated oligomers with terminal donor–acceptor substitution, *Angew. Chem., Int. Ed.*, 2005, **44**, 2482–2506.
26 M. Kivala and F. Diederich, Acetylene-derived strong organic acceptors for planar and nonplanar push–pull chromophores, *Acc. Chem. Res.*, 2009, **42**, 235–248.
27 F. Bureš, Fundamental aspects of property tuning in push–pull molecules, *RSC Adv.*, 2014, **4**, 58826–58851.
28 C. Pigot, G. Noirbent, D. Brunel and F. Dumur, Recent advances on push–pull organic dyes as visible light photoinitiators of polymerization, *Eur. Polym. J.*, 2020, **133**, 109797.
29 A. Abbotto, L. Beverina, R. Bozio, S. Bradamante, C. Ferrante, G. A. Pagani and R. Signorini, Push–pull organic chromophores for frequency-upconverted lasing, *Adv. Mater.*, 2000, **12**, 1963–1967.
30 H.-T. Feng, J. Zeng, P.-A. Yin, X.-D. Wang, Q. Peng, Z. Zhao, J. W. Lam and B. Z. Tang, Tuning molecular emission of organic emitters from fluorescence to phosphorescence through push–pull electronic effects, *Nat. Commun.*, 2020, **11**, 2617.
31 E. V. Verbitskiy, G. L. Rusinov, O. N. Chupakhin and V. N. Charushin, Design of fluorescent sensors based on azaheterocyclic push–pull systems towards nitroaromatic explosives and related compounds: A review, *Dyes Pigm.*, 2020, **180**, 108414.
32 P. Kaur and K. Singh, Second-order nonlinear polarizability of push–pull chromophores. A decade of progress in donor-π-acceptor materials, *Chem. Rec.*, 2022, **22**, e202200024.
33 Y. Patil, H. Butenschön and R. Misra, Tetracyanobutadiene bridged push–pull chromophores: Development of new generation optoelectronic materials, *Chem. Rec.*, 2023, **23**, e202200208.
34 M. F. Abdollahi and Y. Zhao, Recent advances in dithiafulvenyl-functionalized organic conjugated materials, *New J. Chem.*, 2020, **44**, 4681–4693.
35 A. Yoshimura, H. Kimura, K. Kagawa, M. Yoshioka, T. Itou, D. Vasu, T. Shirahata, H. Yorimitsu and Y. Misaki, Synthesis

and properties of tetrathiafulvalenes bearing 6-aryl-1,4-dithiafulvenes, *Beil. J. Org. Chem.*, 2020, **16**, 974–981.

36 M. Dekhtiarenko, S. Krykun, V. Carré, F. Aubriet, D. Canevet, M. Allain, Z. Voitenko, M. Sallé and S. Goeb, Tuning the structure and the properties of dithiafulvene metalla-assembled tweezers, *Org. Chem. Front.*, 2020, **7**, 2040–2046.

37 V. Bliksted Roug Pedersen, J. Granhøj, A. Erbs Hillers-Bendtsen, A. Kadziola, K. V. Mikkelsen and M. Brøndsted Nielsen, Fulvalene-based polycyclic aromatic hydrocarbon ladder-type structures: Synthesis and properties, *Chem. – Eur. J.*, 2021, **27**, 8315–8324.

38 R. Andreu, M. J. Blesa, L. Carrasquer, J. Garn, J. Orduna, R. Alcala and B. Villacampa, 1,3-Dithiole based quinoid systems: multiply proaromatic NLO-phores, *Phosphorus, Sulfur Silicon Relat. Elem.*, 2005, **180**, 1473–1474.

39 R. Andreu, M. J. Blesa, L. Carrasquer, J. Garn, J. Orduna, B. Villacampa, R. Alcalá, J. Casado, M. C. Ruiz Delgado and J. T. López Navarrete, *et al.*, Tuning first molecular hyperpolarizabilities through the use of proaromatic spacers, *J. Am. Chem. Soc.*, 2005, **127**, 8835–8845.

40 S. Amriou, C. Wang, A. S. Batsanov, M. R. Bryce, D. F. Perepichka, E. Ort, R. Viruela, J. Vidal-Gancedo and C. Rovira, The interplay of inverted redox potentials and aromaticity in the oxidized states of new π-electron donors: 9-(1,3-dithiol-2-ylidene)fluorene and 9-(1,3-dithiol-2-ylidene)-thioxanthene derivatives, *Chem. – Eur. J.*, 2006, **12**, 3389–3400.

41 F. Shahrokhi, R. F. Estabragh and Y. Zhao, Synthesis and comparative studies of K-region functionalized pyrene derivatives, *New J. Chem.*, 2020, **44**, 16786–16794.

42 A. Pratt, The photochemistry of imines, *Chem. Soc. Rev.*, 1977, **6**, 63–81.

43 C. D. Meyer, C. S. Joiner and J. F. Stoddart, Template-directed synthesis employing reversible imine bond formation, *Chem. Soc. Rev.*, 2007, **36**, 1705–1723.

44 M. E. Belowich and J. F. Stoddart, Dynamic imine chemistry, *Chem. Soc. Rev.*, 2012, **41**, 2003–2024.

45 R. D. Patil and S. Adimurthy, Catalytic methods for imine synthesis, *Asian J. Org. Chem.*, 2013, **2**, 726–744.

46 K. Acharyya and P. S. Mukherjee, Organic imine cages: Molecular marriage and applications, *Angew. Chem., Int. Ed.*, 2019, **58**, 8640–8653.

47 C. Qian, L. Feng, W. L. Teo, J. Liu, W. Zhou, D. Wang and Y. Zhao, Imine and imine-derived linkages in two-dimensional covalent organic frameworks, *Nat. Rev. Chem.*, 2022, **6**, 881–898.

48 C. Prinzisky, I. Meyenburg, A. Jacob, B. Heidelmeier, F. Schröder, W. Heimbrodt and J. Sundermeyer, Optical and electrochemical properties of anthraquinone imine based dyes for dye-sensitized solar cells, *Eur. J. Org. Chem.*, 2016, 756–767.

49 M.-D. Damaceanu, C.-P. Constantin and L. Marin, Insights into the effect of donor-acceptor strength modulation on physical properties of phenoxazine-based imine dyes, *Dyes Pigm.*, 2016, **134**, 382–396.

50 M. Tumer, F. Tumer, M. Kose, S. A. Gungor, S. Akar, I. Demirtas and G. Ceyhan, Structural characterizations, photophysical and biological properties of Disperse black 9 dye and π-extended imine derivatives, *Dyes Pigm.*, 2018, **154**, 62–74.

51 C. E. de Melo, C. R. Nicoleti, M. C. Rezende, A. J. Bortoluzzi, R. S. Heying, R. S. Oliboni, G. F. Caramori and V. G. Machado, Reverse solvatochromism of imine dyes comprised of 5-nitrofuran-2-yl or 5-nitrothiophen-2-yl as electron acceptor and phenolate as electron donor, *Chem. – Eur. J.*, 2018, **24**, 9364–9376.

52 J. Nakayama, N. Matsumaru and M. Hoshino, Preparation of stable quinone methide imines, *J. Chem. Soc., Chem. Commun.*, 1981, 565–566.

53 B. R. Rani, M. Rahman and U. Bhalerao, A facile one pot synthesis of 3-substituted-1,2,4-triazolo[4,3-b][4,1,2]benzothiadiazine-8-ones, *Org. Prep. Proced. Inter.*, 1991, **23**, 157–162.

54 U. T. Bhalerao, C. Muralikrishna and B. R. Rani, Laccase enzyme catalysed efficient synthesis of 3-substituted-1,2,4-triazoto(4,3-b)(4,1,2)benzothiadiazine-8-ones, *Tetrahedron*, 1994, **50**, 4019–4024.

55 B. A. Koscher, R. B. Canty, M. A. McDonald, K. P. Greenman, C. J. McGill, C. L. Bilodeau, W. Jin, H. Wu, F. H. Vermeire, B. Jin, T. Hart, T. Kulesza, S.-C. Li, T. S. Jaakkola, R. Barzilay, R. Gómez-Bombarelli, W. H. Green and K. F. Jensen, Autonomous, multiproperty-driven molecular discovery: From predictions to measurements and back, *Science*, 2023, **382**, eadi1407.

56 C. A. Christensen, A. S. Batsanov and M. R. Bryce, Thiolated π-extended tetrathiafulvalenes: Versatile multifunctional π-systems, *J. Org. Chem.*, 2007, **72**, 1301–1308.

57 G. Steimecke, H.-J. Sieler, R. Kirmse and E. Hoyer, 1,3-Dithiole-2-thione-4,5-dithiolate from darbon disulfide and alkali metal, Phosphorus, *Sulfur, Rel. Elem.*, 1979, **7**, 49–55.

58 G. Chen, I. Mahmud, L. N. Dawe, L. M. Daniels and Y. Zhao, Synthesis and properties of conjugated oligoyne-centered π-extended tetrathiafulvalene analogues and related macromolecular systems, *J. Org. Chem.*, 2011, **76**, 2701–2715.

59 M. K. Nazeeruddin, A. Kay, I. Rodicio, R. Humphry-Baker, E. Muller, P. Liska, N. Vlachopoulos and M. Gratzel, Conversion of light to electricity by *cis*-X2bis(2,2′-bipyridyl-4,4′-dicarboxylate)ruthenium(II) charge-transfer sensitizers (X = Cl–, Br–, I –, CN–, and SCN–) on nanocrystalline TiO2 electrodes, *J. Am. Chem. Soc.*, 1993, **115**, 6382–6390.

60 A. Hagfeldt, G. Boschloo, L. Sun, L. Kloo and H. Pettersson, Dye-sensitized solar cells, *Chem. Rev.*, 2010, **110**, 6595–6663.

61 A. Ajayaghosh, Chemistry of squaraine-derived materials: near-IR dyes, low band gap systems, and cation sensors, *Acc. Chem. Res.*, 2005, **38**, 449–459.

62 A. Mishra, R. K. Behera, P. K. Behera, B. K. Mishra and G. B. Behera, Cyanines during the 1990s: a review, *Chem. Rev.*, 2000, **100**, 1973–2012.

63 E. Buncel and S. Rajagopal, Solvatochromism and solvent polarity scales, *Acc. Chem. Res.*, 1990, **23**, 226–231.

64 C. Reichardt, Solvatochromic dyes as solvent polarity indicators, *Chem. Rev.*, 1994, **94**, 2319–2358.

65 C.-P. Lee, R. Y.-Y. Lin, L.-Y. Lin, C.-T. Li, T.-C. Chu, S.-S. Sun, J. T. Lin and K.-C. Ho, Recent progress in organic sensitizers

for dye-sensitized solar cells, *RSC Adv.*, 2015, **5**, 23810–23825.

66 P. P. Kumavat, P. Sonar and D. S. Dalal, An overview on basics of organic and dye sensitized solar cells, their mechanism and recent improvements, *Renew. Sustain. Energy Rev.*, 2017, **78**, 1262–1287.

67 K. Sun, P. Xiao, F. Dumur and J. Lalevée, Organic dye-based photoinitiating systems for visible-light-induced photopolymerization, *J. Polym. Sci.*, 2021, **59**, 1338–1389.

68 Y. Ooyama and Y. Harima, Photophysical and electrochemical properties, and molecular structures of organic dyes for dye-sensitized solar cells, *Chem. Phys. Chem.*, 2012, **13**, 4032–4080.

69 D. Yates, Infrared studies of the surface hydroxyl groups on titanium dioxide, and of the chemisorption of carbon monoxide and carbon dioxide, *J. Phys. Chem.*, 1961, **65**, 746–753.

70 M. Primet, P. Pichat and M. V. Mathieu, Infrared study of the surface of titanium dioxides. I. Hydroxyl groups, *J. Phys. Chem.*, 1971, **75**, 1216–1220.

71 K. S. Finnie, D. J. Cassidy, J. R. Bartlett and J. L. Woolfrey, IR spectroscopy of surface water and hydroxyl species on nanocrystalline TiO_2 films, *Langmuir*, 2001, **17**, 816–820.

72 C. Bannwarth, S. Ehlert and S. Grimme, GFN2-xTBAn accurate and broadly parametrized self-consistent tight-binding quantum chemical method with multipole electrostatics and density-dependent dispersion contributions, *J. Chem. Theor. Comput.*, 2019, **15**, 1652–1671.

73 S. Grimme, Exploration of chemical compound, conformer, and reaction space with meta-dynamics simulations based on tight-binding quantum chemical calculations, *J. Chem. Theor. Comput.*, 2019, **15**, 2847–2862.

74 P. Pracht, F. Bohle and S. Grimme, Automated exploration of the low-energy chemical space with fast quantum chemical methods, *Phys. Chem. Chem. Phys.*, 2020, **22**, 7169–7192.

75 M. J. Frisch, G. W. Trucks, H. B. Schlegel, G. E. Scuseria, M. A. Robb, J. R. Cheeseman, G. Scalmani, V. Barone, G. A. Petersson, H. Nakatsuji, X. Li, M. Caricato, A. V. Marenich, J. Bloino, B. G. Janesko, R. Gomperts, B. Mennucci, H. P. Hratchian, J. V. Ortiz, A. F. Izmaylov, J. L. Sonnenberg, D. Williams-Young, F. Ding, F. Lipparini, F. Egidi, J. Goings, B. Peng, A. Petrone, T. Henderson, D. Ranasinghe, V. G. Zakrzewski, J. Gao, N. Rega, G. Zheng, W. Liang, M. Hada, M. Ehara, K. Toyota, R. Fukuda, J. Hasegawa, M. Ishida, T. Nakajima, Y. Honda, O. Kitao, H. Nakai, T. Vreven, K. Throssell, J. A. Montgomery, Jr., J. E. Peralta, F. Ogliaro, M. J. Bearpark, J. J. Heyd, E. N. Brothers, K. N. Kudin, V. N. Staroverov, T. A. Keith, R. Kobayashi, J. Normand, K. Raghavachari, A. P. Rendell, J. C. Burant, S. S. Iyengar, J. Tomasi, M. Cossi, J. M. Millam, M. Klene, C. Adamo, R. Cammi, J. W. Ochterski, R. L. Martin, K. Morokuma, O. Farkas, J. B. Foresman and D. J. Fox, *Gaussian 16 Revision C.01*, 2016, Gaussian Inc., Wallingford CT.

76 C. Barraclough, J. Lewis and R. Nyholm, The stretching frequencies of metal–oxygen double bonds, *J. Chem. Soc.*, 1959, 3552–3555.

77 M. N. Alekshun and S. B. Levy, Molecular mechanisms of antibacterial multidrug resistance, *Cell*, 2007, **128**, 1037–1050.

78 C. Walsh, Molecular mechanisms that confer antibacterial drug resistance, *Nature*, 2000, **406**, 775–781.

79 E. D. Brown and G. D. Wright, Antibacterial drug discovery in the resistance era, *Nature*, 2016, **529**, 336–343.

80 F. Gao, T. Wang, J. Xiao and G. Huang, Antibacterial activity study of 1,2,4-triazole derivatives, *Eur. J. Med. Chem.*, 2019, **173**, 274–281.

81 B. Zhang, Comprehensive review on the anti-bacterial activity of 1,2,3-triazole hybrids, *Eur. J. Med. Chem.*, 2019, **168**, 357–372.

82 J. Li and J. Zhang, The antibacterial activity of 1,2,3-triazole- and 1,2,4-triazole-containing hybrids against Staphylococcus aureus: An updated review (2020-present), *Curr. Top. Med. Chem.*, 2022, **22**, 41–63.

83 P. Yang, J.-B. Luo, Z.-Z. Wang, L.-L. Zhang, J. Feng, X.-B. Xie, Q.-S. Shi and X.-G. Zhang, Synthesis, molecular docking, and evaluation of antibacterial activity of 1,2,4-triazole-norfloxacin hybrids, *Bioorg. Chem.*, 2021, **115**, 105270.

84 M. Balouiri, M. Sadiki and S. K. Ibnsouda, Methods for in vitro evaluating antimicrobial activity: A review, *J. Pharm. Anal.*, 2016, **6**, 71–79.

85 Z. Xu, J. Wu, B. Lovely, Y. Li, M. Ponder, K. Waterman, Y.-T. Kim, D. Shuai, Y. Yin and H. Huang, Visible light-activated dye-sensitized TiO_2 antibacterial film: A novel strategy for enhancing food safety and quality, *J. Hazard. Mater.*, 2024, **480**, 136296.

86 (*a*) CCDC 2132937: Experimental Crystal Structure Determination, 2026, DOI: **10.5517/ccdc.csd.cc29lhfv**; (*b*) CCDC 2132938: Experimental Crystal Structure Determination, 2026, DOI: **10.5517/ccdc.csd.cc29lhgw**; (*c*) CCDC 2132939: Experimental Crystal Structure Determination, 2026, DOI: **10.5517/ccdc.csd.cc29lhhx**; (*d*) CCDC 2132940: Experimental Crystal Structure Determination, 2026, DOI: **10.5517/ccdc.csd.cc29lhjy**; (*e*) CCDC 2132941: Experimental Crystal Structure Determination, 2026, DOI: **10.5517/ccdc.csd.cc29lhkz**; (*f*) CCDC 2132942: Experimental Crystal Structure Determination, 2026, DOI: **10.5517/ccdc.csd.cc29lhl0**; (*g*) CCDC 2132943: Experimental Crystal Structure Determination, 2026, DOI: **10.5517/ccdc.csd.cc29lhm1**; (*h*) CCDC 2132944: Experimental Crystal Structure Determination, 2026, DOI: **10.5517/ccdc.csd.cc29lhn2**.